Dynamic behaviour of auxetic gradient composite hexagonal honeycombs

L. Boldrin[1], S. Hummel[1], F. Scarpa[1,2]*, D. Di Maio[1,2], C. Lira[1], M. Ruzzene[3], C. D. L. Remillat[4] T. C. Lim[5], R. Rajasekaran[6], S. Patsias[6]

[1]*Advanced Composites Centre for Innovation and Science (ACCIS), University of Bristol, Bristol BS8 1TR, UK*

[2]*Dynamics and Control Research Group, Faculty of Engineering, University of Bristol, Bristol BS8 1TR, UK*

[3]*D. Guggenheim School of Aerospace Engineering, Georgia Institute of Technology, Atlanta, GA 30332*

[4]*Aerospace Engineering, Queens School of Engineering, University of Bristol, University Walk, Bristol BS8 1TR, UK*

[5]*School of Science and Technology, SIM University, Singapore, Singapore*

[6]*Mechanical Methods, Rolls-Royce plc, PO Box 31, DE24 8BJ Derby, UK*

Abstract

The paper describes a vibroacoustics analysis of auxetic gradient honeycomb composite structures with hexagonal configurations. We examine two classes of gradient cellular layout - one with continuously varying internal cell angle, the other with gradient cell wall aspect ratio across the surface of the honeycomb panel. The structural dynamics behaviour of the two gradient honeycomb configurations is simulated using full-scale Finite Elements and Component Mode Synthesis (CMS) substructuring. Samples of the gradient honeycombs have been manufactured by means of 3D printing techniques, and subjected to modal analysis using scanning laser vibrometry. We observe a general good comparison between the numerical and the experimental results. A numerical parametric analysis shows the effect of the gradient topology upon the average mobility and general vibroacoustics response of these particular cellular structures.

Keywords: Modal analysis, Auxetic, Honeycomb, gradient cellular structure

1. Introduction

Sandwich structures are still widely used in a variety of airframe structures such as fixed and rotary wing designs, as well as in spacecraft constructions.

---

*Corresponding author

The core of sandwich panels is mainly represented by honeycombs with regular hexagonal or overexpanded configurations, although different layouts have been introduced in the market during the last twenty years, notably flexcores and toroidal honeycombs [1, 2]. As a subset of cellular structures, auxetic (i.e. negative Poisson's ratio - $\nu < 0$) honeycombs have also received some interest within the research community, due to their peculiar mechanical characteristics like sinclastic curvature, general increase of transverse shear modulus, indentation and flatwise compressive stiffness at low relative densities [3, 4, 5]. Honeycomb tessellations that exhibit in-plane negative Poisson's ratio (NPR) values have been developed from re-entrant configurations based on the classical hexagonal butterfly honeycomb geometry [6], which have been also expanded in the domain of zero Poisson's ratio with the accordion honeycomb configuration [7]. The modal and sound transmissibility properties of these auxetic honeycombs have been evaluated in [8], and their viscoelastic dissipation properties in [9, 10]. Other honeycomb auxetic configurations have also been produced from non-centre-symmetric chiral topologies [4, 11, 12] and star-shaped layouts [13]. The vast majority of the honeycomb configurations described in open literature are characterised by a single unit cell with fixed geometry, repeated in two dimensions along a periodic pattern across the surface of a panel. These fixed configurations allow to reach a single set of radiuses of curvature when a honeycomb panel is bent, the anticlastic (saddle-shaped) for positive ν, cylindrical for $\nu = 0$, or sinclastic (dome-shaped) for $\nu < 0$. The presence of a continuous varying (or gradient) pattern of unit cells across the honeycomb panel surface would however allow more complex combinations of localised curvatures during deformation, making also possible to produce sandwich panels and shells adapted to complex shapes. A pioneering concept of gradient honeycomb was proposed by Lim in 2002 [14], with a gradient distribution of internal cell angles that provides an in-plane shearing effect during loading. Some of the authors of this paper have also developed another gradient geometry based on a continuous varying thickness distribution of the horizontal ribs in centre-symmetric cells [15]. This gradient configuration shows an increased shear modulus per unit weight compared to the pristine layout (where the thickness of the horizontal ribs is fixed), and a reduction of the honeycomb anisotropy along preferential directions. Material properties of functionally graded Voronoi cellular structures based on gradients of density and subjected to uniaxial and biaxial stress state have been discussed by Ajdari et al [16]. The authors have shown that the overall effective elastic modulus and yield strength of these particular cellular tessellations increase by increasing the density gradient, and that cellular configurations with higher density gradient exhibit lower steady-state creep rate compared to tessellations with lower density distributions. Cui et al. [17] have observed that a functionally graded foam can exhibit superior energy absorption capabilities compared to a uniform foam topology layout having the same mass. The energy absorption of functionally graded regular hexagonal honeycombs has been observed to be highly sensitive to the type of gradient topology used, especially under very high dynamic compressive loading and during the early stages of crushing [18]. Gradient and graded-type open cell foams produced and

2

characterised by Alderson et al. have shown overall unusual deformation mechanisms under tensile loading [19]. Gradient cellular tessellations with graded cell-wall aspect ratios and internal cell angles have been studied by Hou et al. as potential fillers for sandwich beams subjected to three-point bending tests [20]. Always in terms of energy absorption under dynamic loading, graded auxetic-conventional honeycombs produced with Kirigami (Origami plus cuts) techniques have exhibit significant absorption properties under edgewise loading, with different deformation mechanisms occurring whether the loaded side of the honeycomb was the conventional or the auxetic one [21]. The tuning and control of the thermal conductivity and transport properties through gradient centresymmetric cellular structures has been also proposed by Zhang et al. [22].

All the above cited papers related to gradient cellular structure concern the mechanical and multiphysics performance of these peculiar cellular topologies. However, little has been done about the evaluation of the vibrational performance of these gradient configurations. Graded hexagonal honeycomb sequences have been also used to minimise the dynamic deformation of aeroengine fan blades for the first three modes (flexural and torsional) [23]. Xu et al. have observed a significant reduction of the vibration transmissibility under in-plane dynamic forced vibration when using gradient tri-chiral honeycomb concepts [24], demonstrating that the gradient cellular configuration creates a significant disruption of the pass-stop band wave propagation behaviour typical of the periodic pattern observed in other centresymmetric auxetic and chiral configurations [25]. While the modal properties and dynamic response of general fixed unit cell geometry honeycomb structures have sufficiently well investigated [26, 27], no similar analysis has been attempted so far to evaluate the vibroacoustics response of gradient centresymmetric cellular structures with auxetic characteristics, both from the numerical and experimental point of view. This paper aims at filling this gap existing in open literature. The focus of the paper is also about the vibroacoustics performance of these peculiar cellular configurations, and not about considering the effect of the presence of skins like in classical sandwich configurations, which leads to the transverse shear deformation of the core dominating the lower modes [28, 29].

In this work the modal and structural dynamics response of cellular panels made of auxetic gradient honeycombs with centresymmetric unit cells is evaluated using numerical and experimental techniques. From the numerical point of view the gradient panels are modeled using both reduced order models based on Component Mode Synthesis (CMS) and full-scale Finite Element models. The CMS method allows in theory to substructure in an efficient manner the gradient geometry, sampling each supermodel unit as a single column of the gradient honeycombs and making therefore a parametric design less computationally expensive for these complex structures. As it will be demonstrated, the CMS approach applied to these particular complex cellular structures demonstrates his reliability in terms of predictions of the fundamental modes of the cellular panel, however the type of core material adopted (isotropic or orthotropic) does affect the efficiency of the CMS simulations. Full-scale Finite Element and

3

CMS models do however show a good comparison with experimental results conducted on gradient panel samples produced with 3D printing techniques. A parametric analysis is also carried how to understand the effect of different geometry parameters of the gradient topologies over the average mobility of the cellular panels, an indication of the modal density behaviour of these structures. To the best of the Authors' knowledge this is the first time that a combined numerical and experimental work has been carried out about the modal and dynamic properties of these gradient cellular structures.

2. Gradient topologies, simulations, manufacturing and testing

The aspect-ratio topology (coded as #1 [20]) consists in a continuous varying horizontal rib length h for each row (Fig. 4). The base configuration is represented by a re-entrant unit-cell with parameters $\alpha = h_0/l_0 = 1$ ($l_0 = 10$ mm) and angle $\theta_0 = -10°$. The vertical span $d = l_0 \cos(-10°)$ is kept constant along the global y-direction. From the starting position the horizontal length h is varied as $h_1, h_2, ..., h_{11}$ with a fixed increment $\Delta h = 0.05 h_0$. The horizontal span of each column $dx = 2(l_0 \sin\theta_0 + h_0)$ and the cell-wall thickness $t = 0.5$ mm are fixed in the present configuration. The fundamental re-entrant shape of the cells is kept along the y-direction, with the gradient providing a dilation of the "butterfly" units, which translates into an increasing aspect ratio $\alpha = h/l$ along the y-direction. The panel core depth b is constant, equal to 37 mm for the test case considered. As observed in other gradient cellular structures, the number of cells used in each panel (7 X 8) allows to obtain a mechanical behaviour close to the asymptotic (first order) homogenised one [15]. The other graded topology (coded as #2 [20]) consists instead in a continuously varying aspect ratio $\alpha = h/l$ versus the internal cell angle θ. The cell-wall length l_0 is fixed over the whole surface of the cellular panel, and the internal angle θ is continuously varied along the y-direction, with $\theta = -25°$ and $\theta = 30°$ assumed as angular limits at the bottom and top sides of the panel respectively for the test case considered (Fig. 4). A gradient law can be mathematically expressed as $\theta = -25° + \theta_\xi \cdot \xi^i$, where the non-dimensional coordinate $\xi = [0, 1]$ along y-direction is introduced. The present angle-graded topology reported in Fig. 4 has a linear gradient progression (i.e. i=1). The cell wall slenderness ratio $\beta = t/l_0$ is constant through the panel, whereas the aspect ratio $\alpha = 1$ assumed at the bottom row for $\theta = -25°$ progressively reduces with increasing θ. The variation from positive to negative internal cell angles leads to an increase of the local relative density. The two graded panels have common value of base cell-wall length l_0, cell-wall thickness t and panel depth b.

Full-scale finite-element models of the test case graded topologies have been developed using the commercial Finite Element code ANSYS 11.0. The elements used are 8-node structural elastic shells (SHELL93) with six nodal degrees of freedom (translations and rotations along the three Cartesian axis). After a convergence analysis on the modal frequencies of the samples, an average element size equal to $b/5$ has been employed for all the models. Reduced order models of the gradient lattices have been developed using a Component Mode Synthesis

(CMS) free-free interface approach (Fig. 4) [30, 31]. The gradient substructures shown in Fig. 4 can be assembled in a linear chain, making possible to calculate the natural frequencies of the whole gradient honeycomb. The simulations performed in this work involve the use of 2, 10 or 100 modes to calculate the basis $[\mathbf{\Phi_N}]$ for the CMS approach [30]. In order to mimic the experimental setup, the FE nodes below the region of the clamp were constrained on the front and back surface of the samples in order to simulate the influence of the two washers and their potential influence on the structural dynamic response. The frequency response functions (FRFs) were calculated from the FEA models in the same 24 point locations used within the experiment. Fig. 4 - 4 illustrate the measuring locations and the clamp positions for both samples. The FEA FRFs have been used to extrapolated the average mobility of the gradient cellular configurations for the parametric analysis.

The gradient lattice samples have been manufactured using a Fusion Deposition Moulding (FDM) 3D printing technique (Stratasys Dimension Elite ® - Serial number 067557). The samples made from ABSPlus ® polymer had uniform nominal cell-wall thickness of 0.5 mm (minimum allowed thickness of 0.5 mm). The core material properties of the lattices were determined from tensile ASTM D638-08 tests on dog-bone specimens produced with the same FDM technique along the layer-wise and transverse directions used by the 3D printing manufacturing process. The ABS dog-bone specimens showed a quasi special orthotropic behavior [2], with Young's moduli $E_y = 2.02\,\text{GPa}$ and $E_z = 1.54\,\text{GPa}$. The Poisson's ratios, determined using a video-estensometer technique based on edge detection method (Messphysik GmbH), were $\nu_{yz} = 0.43$ and $\nu_{zy} = 0.41$ respectively. The shear modulus was estimated using an equivalent isotropic material made by the geometric mean of the Young's moduli and Poisson's ratios $E_{eq} = \sqrt{E_y E_z}$ and $\nu_{eq} = \sqrt{\nu_{yz}\nu_{zy}}$, and using the classical definition $G_{eq} = E_{eq}/2/\left(1 + \nu_{eq}\right)$, leading to a shear modulus value of 618 MPa. The use of an equivalent isotropic material model has yielded satisfactory comparison between numerical and experimental mechanical static results for similar types of 3D printed cellular structures [15], and it would be interesting to observe if the adoption of an isotropic material model for the core could still provide an acceptable approximation to represent the gradient cellular structures. An estimation of the hysteretic loss factor of the ABS plastics material has been obtained using a Dynamic Mechanical Analyser (Metravib RDS VA2000) under 3-point bending loading at room temperature and 1.5 Hz of excitation (constant dynamic strain of 10^{-4}). The measured loss factor ($\eta = 0.02$) has been considered as constant within the frequency range of the bandwidth excitation in the full-scale Finite Element models used in the frequency response simulation.

The dynamic tests have been carried out with a random broadband excitation between 5 Hz and 2 kHz. A central clamp was manufactured using two washers linked by a rod, and placed in the middle of the cellular panel (Fig. 4 - 4). The washers were placed on the top and bottom of the cellular panels, and the joining rod was passing through the void on the central cell. Two nuts were fixing the rod to the washers. The central clamp was connected to a PCB 208C03 force transducer (SN 21535), linked to a LDS V406 electrodynamic

shaker through a steel stinger rod. The shaker was driven by a DSP Technology Inc. Siglab 20-42 through a LDS PA100E power amplifier. Each sample was scanned in 24 locations using a Polytec PSV-300F Scanning Laser Vibrometer (SLV). The mobilities detected by the SLV were post-processed using a DFT-based software, in which the structural velocities signals were sampled at 5.1 kHz using 1600 spectral lines, with the time domains filtered using Hanning windows and the FFT computed with 10 complex averages and 50 % of overlap. The operational mode shapes of the gradient cellular structures have been identified from the peaks of the average mobility indicator H_1. Natural frequencies and mode shapes have been extracted using the ICATS modal analysis software. The experimental modal damping ratios were measured with each FRF curve-fit with a Line-Fit algorithm [32].

When the system is subjected to an harmonic excitation $f = f_0 e^{i\omega t}$ the resulting velocity profile is harmonic due to the assumption of the system linearity assumption, and can be expressed as $v = v_0 e^{i\omega t}$. Assuming given excitation frequency ω, the generalized mobility is defined as the ratio of the complex velocity v measured at point i to the complex force f measured at point j :

$$Y_{ij}(\omega) = \frac{v_0(\omega)}{f_0(\omega)} \tag{1}$$

Where the subscripts i, j indicate point locations. When both force and velocity are measured at the same location and along the same direction in a structural system under harmonic excitation, the resulting mobility is named *driving-point* mobility Y_{ij} ($i = j$). If the measuring locations are different, the resulting mobility is named *transfer* mobility Y_{ij} ($i \neq j$) [33]. The average mobility can be defined as:

$$|\frac{\dot{w}}{f}| = \frac{1}{S} \int_{i,j} Y_{ij}(\omega) \, dS_{ij} \tag{2}$$

In (2) S is the overall surface of the cellular panel and dS_{ij} is the infinitesimal surface around which the driving point mobility is calculated. The rationale behind the use of the average mobility is its proportionality to the modal density of sandwich panels [34, 35]. In the present study the mobility of different point locations on the panel have been measured by fixing the location of the excitation force at the geometrical centre of each panel top surface. The calculated mobilities are then *transfer* mobilities measured in 24 different point locations on the panel top surfaces and then used to calculate the average mobility characterizing of the cellular gradient panel. In order to mimic the experimental setup, the nodes below the region of the clamp were constrained on the front and back surface of the samples to simulate the influence of the two washers and their potential influence on the structural dynamic response. The frequency response functions were also calculated for the full-scale FE models in the same 24 point locations adopted in the experiment. Figs. 4 - 4 illustrate the measuring locations and the clamp positions for both specimens.

6

3. Results and discussions

3.1. Comparison between experimental and numerical results

Tables 4 and 4 show the direct comparison between the full scale FE and substructured CMS models for the two gradient topologies with the two material models. The topology #2 shows a significant increase of the resonances across the modal spectrum considered, with the first natural frequency 49 % higher than the analogous one belonging to the sample with gradient topology #1. When the isotropic material model is adopted, the CMS approach is computed with 10 internal modes only. A convergence analysis using 2, 10 and 100 modes has been performed for the orthotropic core material case. The gradient type #1 presents a first natural frequency of 61 Hz with an equivalent isotropic material, and an increase of 3.2 % for the fundamental frequency is observed when the orthotropic material model is adopted. A similar trend is observed when the topology #2 is considered, with the error now varying between 1 % and 4 % for all the other modes considered. The use of an isotropic material model for the core does clearly provide a conservative estimation, and quite interestingly does not represent an approximation as satisfactory as in the case of the transverse shear static load [36, 37]. It is also worth noticing that the use of an equivalent isotropic core material in the CMS models does not provide any noticeable difference from the full-scale FE case. The situation is different when the orthotropic solid case is considered. Although no sizable difference within the CMS-generated results can be observed when using different internal modal basis, the CMS tends to overestimate consistently all the natural frequencies associated to topology #1 by 6.3 % on average compared to the isotropic case, and it is in line with the predictions provided by the full-scale orthotropic models. Sample with gradient #2 shows also a stiffening effect when using the CMS approach by 6.3 % on the fundamental frequency, the other eigenvalues differing between 5.2 % and 7 % compared to the full-scale case. It is also apparent that the different response provided by the CMS approach between the two topologies can be ascribed to the geometries of the samples involved. Although having gradient aspect ratios, sample #1 has always the same re-entrant (butterfly) structure, and the different nodes at the interfaces of the substructures tend to undergo similar rigid body modes. This feature however is not present in sample #2, with the first rows having a butterfly shape that changes into a convex overexpanded honeycomb in the final ones. The interface rigid body modes are different in the various cases, and the number of fixed interface nodes used in the CMS model may be not sufficient to represent in an adequate manner the deformation of the substructured units [30].

The experimental and numerical results for the aspect-ratio topology with a linear gradient are reported in Fig. 4 where the magnitude of the average transfer mobility from 24 sampling locations on the panel is plotted against the excitation frequency bandwidth [50 Hz - 1200 Hz]. Four transmissibility (H_1) peaks for sample #1 have been identified experimentally at 76 Hz, 87 Hz, 94 Hz and 390 Hz (Fig. 4). A good correlation between the experimental and numerical predictions is observed up to 400 Hz. In Table 4 the numerical

predictions and the experimental results shows also a good comparison also in terms of mode shapes and frequencies, with relative errors for the resonance values ranging between 1.1 % and 6.8 % maximum. The difference between the numerical and the experimental findings can be mainly associated to the uncertainties provided by the introduction of the nodal constraints on the top and bottom surfaces in the finite element models to simulate the presence of the two washers in the experimental setup. For the present full-scale models all degrees of freedom of the nodes laying below the region of the clamp on the front and back surface of the structure were constrained, with exception for the DOFs along the excitation direction z. This assumption about the boundary conditions may too conservative and lead to a stiffening effect on the modal behaviour. Moreover, it is important to notice that the use of an average constant loss factor $\eta = 0.02$ introduced in the harmonic analysis based on modal superposition is also an approximation.

The experimental and numerical results for the angle-graded topology with a linear gradient are reported in Fig. 4, in which the average transfer mobility magnitude from 24 sampling locations on the panels is calculated again within the frequency bandwidth [50 Hz - 1200 Hz]. For this type of gradient configuration it is possible to observe three transmissibility peaks at 90 Hz, 169 Hz and 340 Hz (Fig. 4). The Finite Element model provides a quite close prediction with errors of 3%, 3% and 0.3% respectively. Differences between the predicted and measured transmissibility tend to increase above the 400 Hz, in which a higher modal content is observed for the experimental model (Fig. 4). In Table 4 the modal shapes predicted by the Finite Element full-scale modal analysis are compared to the experimental ones. A good correlation can be found for the first three mode shapes, with a more distorted flexural third mode at 341 Hz. It is worth commenting about this particular mode, because it is possible to observe the presence of the two opposite curvatures (positive and negative) when the sample is undergoing a global bending deformation. The presence of the curvatures is related to the gradient transition from the auxetic (butterfly/re-entrant) and convex hexagonal cell configuration through the surface of the panel.

The modal damping ratios (Tables 4 and 4) are very similar for the two sets of gradient configurations, with values ranging from 1.16 % to 5.83 %. It is worth to observe that the highest modal damping ratios occur for the torsional modeshapes, which involve a transverse shear dissipation. Auxetic composite structure do tend to dissipate energy through shear deformation often coupled to tensile loading, as it has been observed in through-the-thickness composites under cyclic high-cycle fatigue loading [38] and earlier on in negative Poisson's ratio cellular materials [39]. Dissipation of shear waves is also responsible for wave attenuation in auxetic foams and the high force absorption during drop-tower impact tests in edgewise auxetic honeycombs [21]. The torsional modes involve the highest levels of modal strain energy dissipation in the cellular panels between the centres and the edges of the honeycomb structures. The other modes show a much more localised distribution of the deformation, with their other modal damping ratios being more or less on line with the hysteretic damp-

ing of the core ABS material, as it is expected in cellular structures made from single phase materials [2].

3.2. Parametric analysis

The benchmarked full-scale Finite Element model has been used to perform a parametric analysis to evaluate the influence of the different gradient configurations on the average mobility response of the two gradient topologies. For sample #1 the baseline periodic tessellation with $\Delta h = 0$ and two graded configurations with $\Delta h = 0.03\, h_0$ and $\Delta h = 0.06\, h_0$ are compared in Fig. 4. The aspect-ratio gradient allows for a dilation of the auxetic "butterfly" unit with an increasing aspect ratio α along the y-direction. The overall density is only weakly affected by the gradient because the parameters d and the column width dx are fixed in this topology. In the simulation the differences in terms of average mobility for the three different cases are minimal, with a maximum discrepancy of 15 % in terms of magnitudes above 800 Hz, slight variations of the peak magnitudes of the first three/four natural frequencies (Fig. 4). Above 880 Hz, the amplitude of the average mobility also tends to increase slightly with the level of $\Delta h/h_0$ used in the gradient topology. These results can be explained by considering that all topologies have approximately the same weight and are almost iso-volume [40]. The nature of the gradient does not change the main topology of the unit cell, which is fixed to the "butterfly" geometry with internal angle $\theta = -10°$, without significant changes to the the unit-cell stiffness along the Cartesian principal directions [20].

The angle-graded topology shows however a different behaviour for the three different gradients described in Fig. 4 and characterised by the variation of the nondimensional parameter ξ^i ($i = 0.5,\ 1,\ 2$). The quadratic gradient describes a panel with negative internal angles θ spanning from $\xi = 0$ to $\xi = 0.7$. The auxetic region of the panel decreases when the linear gradient is used, and further reduction of the fraction of re-entrant unit cells exists for a square-root gradient law. The three topologies exhibit different overall weights, with the highest mass belonging to the quadratic gradient topology (6.3 % more than the linear distribution) and the lowest to the square-root gradient (4.5 % compared again to the linear gradient) because of the reduction of regions with high aspect ratio α and negative θs in the panel. The average transfer mobility within the 50Hz - 1200 Hz bandwidth for the angle-graded topologies is shown in Fig. 4. The angular gradients do provide a significant local relative density distribution along the y-direction and introduce a net change in the unit-cell topology, which moves from auxetic to positive internal cell angle configurations with a subsequent variation of the local unit-cell stiffness along the x, y and z directions [20]. The square-root gradient exhibits the lowest average mobility at frequencies greater than 400 Hz, whilst the quadratic gradient has the highest levels of mobility between the gradient considered in this work (Fig. 4). At lower frequencies (50 Hz - 400 Hz) the quadratic and linear gradient show the maximum peak of their responses at matching frequency, whereas the square-root response shows the fundamental peak at a slightly higher frequency. The quadratic gradient provides an overall decrease of the modal density of the panel below 400 Hz. This

9

decrease is even more significant above 500 Hz, with both the linear and root square gradient providing an average an increase of the density of the H_1 peaks by a factor of three, in particular for the $\xi^{0.5}$ gradient. The overall weight difference and stiffness variation between the three configurations has a net influence on the peak magnitudes of the average mobility and respective frequencies at which such peaks occur. It is interesting at this stage to consider the effect of a different internal constant cell angles versus a given gradient configuration (the linear gradient topology - $\theta \propto \xi$)) as shown in Fig. 4. In this case the two constant internal cell angles ($\theta = -25°$ and $\theta = 30°$) correspond to the angles at the extreme ends of the linear gradient configuration. The negative cell angle value in this configuration is the limit one to avoid the opposite vertex of the cell touching for the specific cell wall aspect ratio used [41]. All panels are characterized by an equal depth b, approximately square aspect-ratio in x, y plane and similar span along x and y-directions, with a maximum 9% difference between the three case studies. The auxetic periodic topology exhibits a weight increase of 19% when compared to the linear angle-graded case, whilst the positive-angle periodic panel shows a 20% weight reduction. While the responses of the fully auxetic and linear graded topologies show a similar trend in the lower frequency range (below 250 Hz), a significant different behaviour is provided by the positive angle periodic topology, with a maximum mobility peak shifted by 40 % to higher frequency and an overall 5 dB lower response when compared to the auxetic solutions (Fig. 4). In general, above 200 Hz the angle graded configuration provides a transition in terms of modal density between the richer full auxetic configuration and the less resonant positive Poisson's ratio uniform cellular topology. Another way to compare the gradient angle topologies is to normalise the mobility by the factor ($[1/M\omega]$), in which M stands for the mass of the panel, and to use the fundamental first peak frequency ω_0 to make the frequency bandwidth nondimensional. This nondimensional approach allows to identify the cellular configurations that provide the lower modal density for a minimum weight, a feature that is quite critical for lightweight and aerospace applications. Also in this case of these simulations, the hysteretic loss factor of the ABS material has been kept the same ($\eta = 0.02$). The results of this normalisation process for the three cellular configurations are shown in Fig. 4. The lowest normalised mobility is the one related to the hexagonal conventional honeycomb ($\theta = 30°$). The peak of the hexagonal regular configuration is also $\tilde{\ } 7$ dB lower, while the full auxetic and the angular gradient configurations exhibit similar values of peak mobility. The regular hexagonal configuration shows overall a very low modal density, with only five peaks present within the range $0 < \omega/\omega_0 < 9$. On the opposite, the full auxetic honeycomb panel shows both the highest magnitudes of the mobility and a very rich modal density within the whole normalised frequency bandwidth considered, with an increase of the number of peaks by a factor of 2.6 compared to the full hexagonal honeycomb panel. The angle gradient topology tends to lower the normalised mobility and also decrease the modal density below $\omega/\omega_0 = 4$, providing almost the same number of nondimensional mobility peaks than the regular hexagonal configuration, albeit with amplitudes between 15 dB and 20 dB higher. At higher nondimensional

10

frequencies ($\omega/\omega_0 > 7$) the auxetic and the gradient configuration tend however to show a similar behaviour with a close modal density.

In terms of modal damping behaviour, the analysis from the single H_1 mobilities yields similar results to the ones observed from the experimental modal analysis shown in Tables 4 and 4. Mobility peaks corresponding to global flexural modes have damping ratios between 1.5 %/2 %. The full auxetic and gradient topologies have a modal damping ratio for the mobility average of 4 % and ~ 3 % for $\omega/\omega_0 \approx 6.4$, which corresponds to a higher order torsional mode (Figure 4). Because of the highest values of the natural frequencies for the hexagonal case, no torsional mode is present in the H_1 response of this panel within the nondimensional frequency bandwidth considered. The flexural modes present in the response of the hexagonal panel have damping ratios close to 1.3 %, quite similar to the ones exhibited by the auxetic configurations.

4. Conclusions

The modal and dynamic behaviour of cellular panels with auxetic gradient cellular structure has been studied using numerical FE and experimental measurements. From the numerical point of view, the use of the Component Mode Synthesis is an efficient approach to predict the vibroacoustics of these gradient cellular panels, however the sensitivity of the results to the material properties used for the core is an aspect to be taken into account, especially when new types of composite and polymeric materials are used to produce these complex configurations due to the advances of manufacturing and additive layer manufacturing techniques. The parametric analysis also shows that only a specific gradient topology does exhibit a significant sensitivity of the dynamic properties versus the change of the gradient geometry. When the mass of the honeycomb panel is however taken into account, the gradient configurations (in particular the angle gradient one) do exhibit a lower modal density compared to fully periodic auxetic configurations, but higher when compared to the classical hexagonal regular honeycomb structures. In a sandwich panel design the face skins would constrain the core to deform principally under transverse shear, therefore the results shown in this paper are representative of a cellular panel and not a sandwich configuration. Nevertheless, these gradient auxetic honeycomb configurations constitute an interesting platform for the multidomain design of sandwich structures from the static and vibroacoustics point of view.

References

[1] D. Zenkert, Introduction to Sandwich Construction, Engineering Materials Advisory Services Ltd, 1997.

[2] L. J. Gibson, M. F. Ashby, Cellular solids: Structure and properties, 2nd Edition, Cambridge: Cambridge University Press, 1997.

[3] R. Lakes, Foam structures with a negative poisson's ratio, Science 235 (4792) (1987) 1038–1040. doi:10.1126/science.235.4792.1038.

[4] D. Prall, R. Lakes, Properties of a chiral honeycomb with a poisson's ratio of -1, International Journal of Mechanical Sciences 39 (3) (1997) 305–314. doi:10.1016/S0020-7403(96)00025-2.

[5] K. E. Evans, A. Alderson, Auxetic materials: Functional materials and structures from lateral thinking!, Advanced Materials 12 (9) (2000) 617–628. doi:10.1002/(SICI)1521-4095(200005)12:9<617::AID-ADMA617>3.0.CO;2-3.

[6] I. Masters, K. Evans, Models for the elastic deformation of honeycombs, Composite Structures 35 (4) (1996) 403 – 422. doi:10.1016/S0263-8223(96)00054-2.

[7] K. R. Olympio, F. Gandhi, Flexible Skins for Morphing Aircraft Using Cellular Honeycomb Cores, Journal of Intelligent Materials Systems and Structures 21 (17) (2010) 1719–1735.

[8] F. Scarpa, G. Tomlinson, Theoretical characteristics of the vibration of sandwich plates with in-plane negative poisson's ratio values, Journal of Sound and Vibration 230 (1) (2000) 45 – 67. doi:10.1006/jsvi.1999.2600.

[9] F. Scarpa, C. D. L. R. Remillat, F. P. Landi, G. R. Tomlinson, Damping modelization of auxetic foams, in: SPIE Volume 3989, Vol. 3989, 2000, pp. 336–344.

[10] G. J. Murray, F. Gandhi, Auxetic honeycombs with lossy polymeric infills for high damping structural materials, Journal of Intelligent Material Systems and Structures 24 (9) (2013) 1090–1104. arXiv:http://jim.sagepub.com/content/24/9/1090.full.pdf+html, doi:10.1177/1045389X13480569.
URL http://jim.sagepub.com/content/24/9/1090.abstract

[11] J. Grima, K. Evans, Auxetic behavior from rotating squares, Journal of Materials Science Letters 19 (17) (2000) 1563–1565. doi:10.1023/A:1006781224002.

[12] A. Alderson, K. Alderson, D. Attard, K. Evans, R. Gatt, J. Grima, W. Miller, N. Ravirala, C. Smith, K. Zied, Elastic constants of 3-, 4- and 6-connected chiral and anti-chiral honeycombs subject to uniaxial in-plane loading, Composites Science and Technology 70 (7) (2010) 1042 – 1048. doi:10.1016/j.compscitech.2009.07.009.

[13] J. N. Grima, R. Gatt, A. Alderson, K. E. Evans, On the potential of connected stars as auxetic systems, Molecular Simulation 31 (13) (2005) 925–935. doi:10.1080/08927020500401139.

[14] T. C. Lim, Functionally graded beam for attaining poisson-curving, Journal of Materials Science Letters 21 (24) (2002) 1899–1901. doi:10.1023/A:1021688009461.

[15] C. Lira, F. Scarpa, Transverse shear stiffness of thickness gradient honeycombs, Composites Science and Technology 70 (6) (2010) 930 – 936. doi:10.1016/j.compscitech.2010.02.007.

[16] A. Ajdari, P. Canavan, H. Nayeb-Hashemi, G. Warner, Mechanical properties of functionally graded 2-d cellular structures: A finite element simulation, Materials Science and Engineering: A 499 (1-2) (2009) 434 – 439. doi:10.1016/j.msea.2008.08.040.

[17] L. Cui, S. Kiernan, M. D. Gilchrist, Designing the energy absorption capacity of functionally graded foam materials, Materials Science and Engineering: A 507 (1-2) (2009) 215 – 225. doi:10.1016/j.msea.2008.12.011.

[18] A. Ajdari, H. Nayeb-Hashemi, A. Vaziri, Dynamic crushing and energy absorption of regular, irregular and functionally graded cellular structures, International Journal of Solids and Structures 48 (3-4) (2011) 506 – 516. doi:10.1016/j.ijsolstr.2010.10.018.

[19] A. Alderson, K. L. Alderson, S. A. McDonald, B. Mottershead, S. Nazare, P. J. Withers, Y. T. Yao, Piezomorphic materials, Macromolecular Materials and Engineering 298 (3) (2013) 318–327. doi:10.1002/mame.201200028. URL http://dx.doi.org/10.1002/mame.201200028

[20] Y. Hou, Y. Tai, C. Lira, F. Scarpa, J. Yates, B. Gu, The bending and failure of sandwich structures with auxetic gradient cellular cores, Composites Part A: Applied Science and Manufacturing 49 (0) (2013) 119 – 131. doi:10.1016/j.compositesa.2013.02.007.

[21] Y. Hou, R. Neville, F. Scarpa, C. Remillat, B. Gu, M. Ruzzene, Graded conventional-auxetic kirigami sandwich structures: Flatwise compression and edgewise loading, Composites Part B: Engineering 59 (0) (2014)

33–42. doi:http://dx.doi.org/10.1016/j.compositesb.2013.10.084.
URL http://www.sciencedirect.com/science/article/pii/S1359836813006598

[22] Y. Zhang, Y. Xu, S. Liu, A fast numerical method for the analysis of the heat transfer performance of graded metallic honeycomb materials, International Journal of Heat and Mass Transfer 79 (0) (2014) 507 – 517. doi:http://dx.doi.org/10.1016/j.ijheatmasstransfer.2014.08.036.
URL http://www.sciencedirect.com/science/article/pii/S0017931014007236

[23] C. Lira, F. Scarpa, R. Rajasekaran, A gradient cellular core for aeroengine fan blades based on auxetic configurations, Journal of Intelligent Material Systems and Structures 22 (9) (2011) 907–917. arXiv:http://jim.sagepub.com/content/22/9/907.full.pdf+html, doi:10.1177/1045389X11414226.
URL http://jim.sagepub.com/content/22/9/907.abstract

[24] X. Shiyin, H. Xiuchang, H. Hongxing, A study on the isolation performance of trichiral lattices with gradient geometry, Journal of Vibration and Control-larXiv:http://jvc.sagepub.com/content/early/2014/07/03/1077546314524261.full.pdf+html, doi:10.1177/1077546314524261.
URL http://jvc.sagepub.com/content/early/2014/07/03/1077546314524261.abstract

[25] A. Spadoni, M. Ruzzene, Structural and acoustic behavior of chiral truss-core beams, Journal of Vibration and Acoustics 128 (2006) 616–626.

[26] S. Jacobs, C. Coconnier, D. DiMaio, F. Scarpa, M. Toso, J. Martinez, Deployable auxetic shape memory alloy cellular antenna demonstrator: design, manufacturing and modal testing, Smart Materials and Structures 21 (7) (2012) 075013.
URL http://stacks.iop.org/0964-1726/21/i=7/a=075013

[27] A. D. Lantada, A. Muslija, J. P. García-Ruíz, Auxetic tissue engineering scaffolds with nanometric features and resonances in the megahertz range, Smart Materials and Structures 24 (5) (2015) 055013.
URL http://stacks.iop.org/0964-1726/24/i=5/a=055013

[28] E. NILSSON, A. NILSSON, {PREDICTION} {AND} {MEASURE-MENT} {OF} {SOME} {DYNAMIC} {PROPERTIES} {OF} {SAND-WICH} {STRUCTURES} {WITH} {HONEYCOMB} {AND} {FOAM} {CORES}, Journal of Sound and Vibration 251 (3) (2002) 409 – 430. doi:http://dx.doi.org/10.1006/jsvi.2001.4007.
URL http://www.sciencedirect.com/science/article/pii/S0022460X01940076

[29] L. Guj, A. Sestieri, Dynamic modeling of honeycomb sandwich panel, Archive of Applied Mechanics 77 (11) (2007) 779–793. doi:10.1007/s00419-007-0121-5.
URL http://dx.doi.org/10.1007/s00419-007-0121-5

[30] R. Craig, A review of substructure coupling methods for dynamic analysis, NASA. Langley Research Center Advances in Engineering Sciences 2.

[31] M. Petyt, Introduction to Finite Element Vibration Analysis, 2nd Edition, Cambridge University Press, 2010.

[32] B. J. Dobson, A straight-line technique for extracting modal properties from frequency response data, Mechanical Signals and Systems Processing 1 (1) (1987) 29–40.

[33] P. Hynnä, Mechanical mobility technique, Tech. Rep. BVAL37-021228, VTT Technical Research Centre of Finland (2002).
URL http://www.vtt.fi/inf/julkaisut/muut/2002/BVAL37-021228.pdf

[34] B. Clarkson, M. Ranky, Modal density of honeycomb plates, Journal of Sound and Vibration 91 (1) (1983) 103 – 118. doi:http://dx.doi.org/10.1016/0022-460X(83)90454-6.
URL http://www.sciencedirect.com/science/article/pii/0022460X83904546

[35] K. Renji, P. Nair, S. Narayanan, {MODAL} {DENSITY} {OF} {COMPOSITE} {HONEYCOMB} {SANDWICH} {PANELS}, Journal of Sound and Vibration 195 (5) (1996) 687 – 699. doi:http://dx.doi.org/10.1006/jsvi.1996.0456.
URL http://www.sciencedirect.com/science/article/pii/S0022460X96904563

[36] C. Lira, P. Innocenti, F. Scarpa, Transverse elastic shear of auxetic multi re-entrant honeycombs, Composite Structures 90 (3) (2009) 314 – 322. doi:10.1016/j.compstruct.2009.03.009.
URL http://www.sciencedirect.com/science/article/pii/S0263822309000865

[37] C. Lira, F. Scarpa, Y. Tai, J. Yates, Transverse shear modulus of silicomb cellular structures, Composites Science and Technology 71 (9) (2011) 1236 – 1241. doi:10.1016/j.compscitech.2011.04.008.
URL http://www.sciencedirect.com/science/article/pii/S0266353811001412

[38] A. Bezazi, W. Boukharouba, F. Scarpa, Mechanical properties of auxetic carbon/epoxy composites: static and cyclic fatigue behaviour, physica status solidi (b) 246 (9) (2009) 2102–2110. doi:10.1002/pssb.200982042.
URL http://dx.doi.org/10.1002/pssb.200982042

[39] C. P. Chen, R. S. Lakes, Dynamic wave dispersion and loss properties of conventional and negative poisson's ratio polymeric materials, Cellular Polymers 8 (343-349).

[40] L. Boldrin, F. Scarpa, R. Rajasekaran, Thermal conductivities of iso-volume centre-symmetric honeycombs, Composite Structures 113 (0) (2014) 498 – 506. doi:http://dx.doi.org/10.1016/j.compstruct.2014.03.013.
URL http://www.sciencedirect.com/science/article/pii/S0263822314001160

[41] F. Scarpa, P. Panayiotou, G. Tomlinson, Numerical and experimental uniaxial loading on in-plane auxetic honeycombs, The Journal of Strain Analysis for Engineering Design 35 (5) (2000) 383–388. doi:10.1243/0309324001514152.

Table 1: Sample #1. Comparison of natural frequencies extracted using CMS and un-substructured (full models), with isotropic and orthotropic material properties.

Full isotropic [Hz]	CMS isotropic [Hz]	Full orthotropic [Hz]	CMS 10 modes orthotropic [Hz]	CMS 100 modes orthotropic [Hz]	CMS 2 modes orthotropic in [Hz]
61	61	67	67	67	67
78	78	81	81	81	81
90	90	95	98	98	98
115	115	119	127	127	127
126	126	130	139	139	139
133	133	138	145	145	145
162	162	168	179	180	179
201	201	211	223	224	223
212	212	220	234	235	234
219	219	227	240	240	240
220	220	228	242	243	242
229	229	238	250	250	250
244	244	255	270	271	270
274	274	294	303	303	303
284	284	302	313	315	313

Table 2: Sample #2. Natural frequencies extracted from CMS and un-substructured (Full) models with isotropic and orthotropic core properties.

Full isotropic [Hz]	CMS isotropic [Hz]	Full orthotropic [Hz]	CMS 10 modes orthotropic [Hz]	CMS 100 modes orthotropic [Hz]	CMS 2 modes orthotropic [Hz]
91	91	95	100	100	100
125	125	129	138	138	138
144	144	153	157	157	157
168	169	174	186	186	187
178	178	185	196	196	196
215	215	222	235	235	235
246	246	254	270	270	270
251	251	262	277	277	277
264	264	275	289	289	289
302	303	316	334	334	334
331	331	341	363	363	363
337	337	348	374	374	374
357	357	370	391	391	391
358	358	373	394	394	395
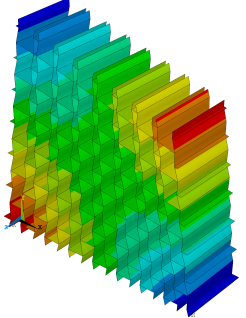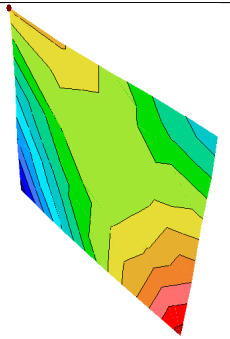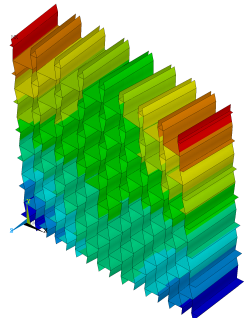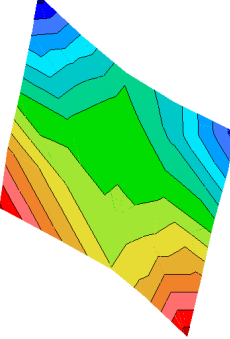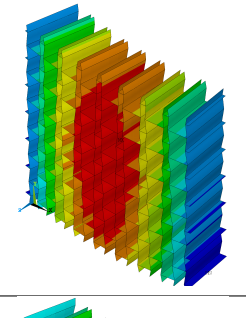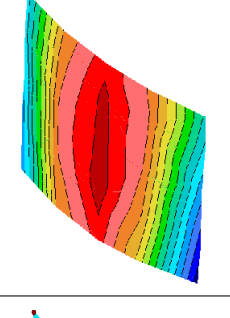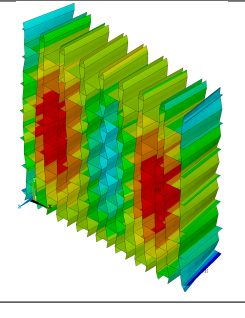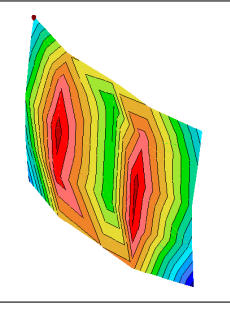
FEA [Hz]	Experimental [Hz]	Modal loss factor [%]	FEA modeshape	Experimental modeshape
67	63	5.6		
81	87	1.55		
95	94	1.16		
393	390	1.45		

Table 3: Comparison between experimental and finite-element modeshapes for sample #1.
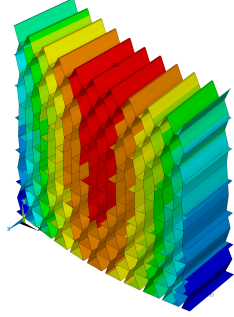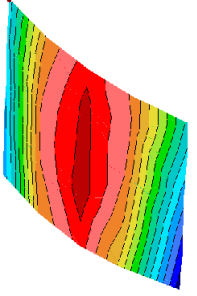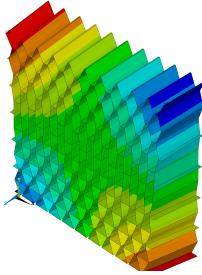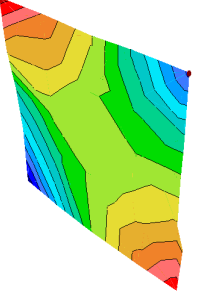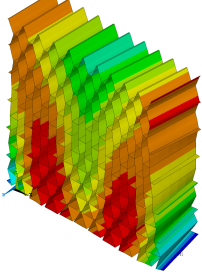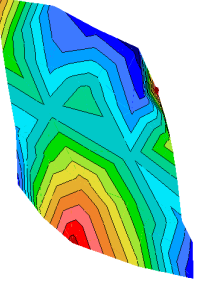
FEA [Hz]	Experimental [Hz]	Modal loss factor [%]	FEA modeshapes	Experimental modeshapes
95	93	1.16		
153	159	5.83		
341	340	1.45		

Table 4: Comparison between experimental and finite-element natural frequencies and mode-shapes for sample #2.
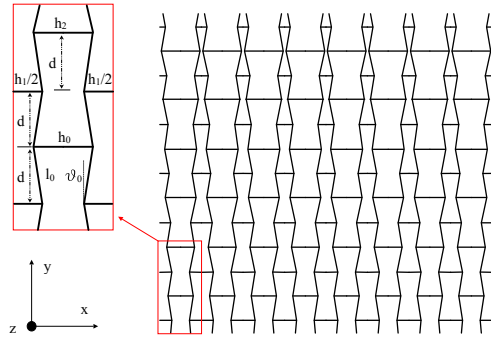
Figure 1: Aspect-ratio graded topology #1 with linear gradient along the h parameter.
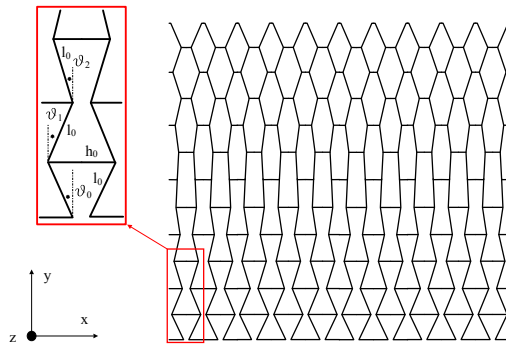
Figure 2: Angle-graded topology with linear gradient in θ (#2). Oblique cell-wall length L_1 is fixed with varying internal angle θ.
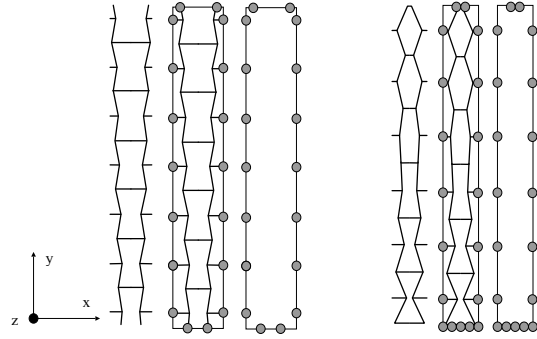
Figure 3: Super elements for subtracturing in samples 1 and 2.
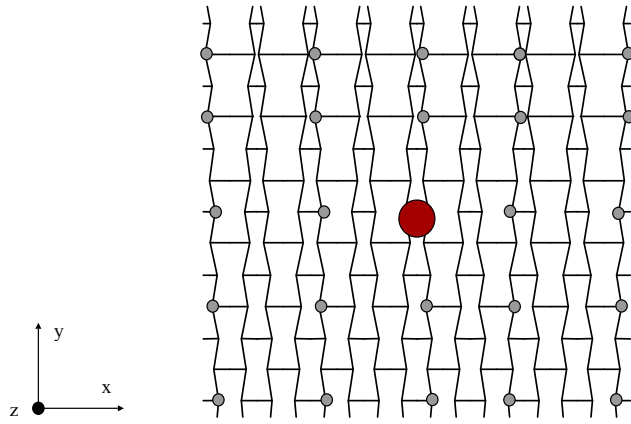
Figure 4: Locations of the measurement points and central clamp for sample 1.
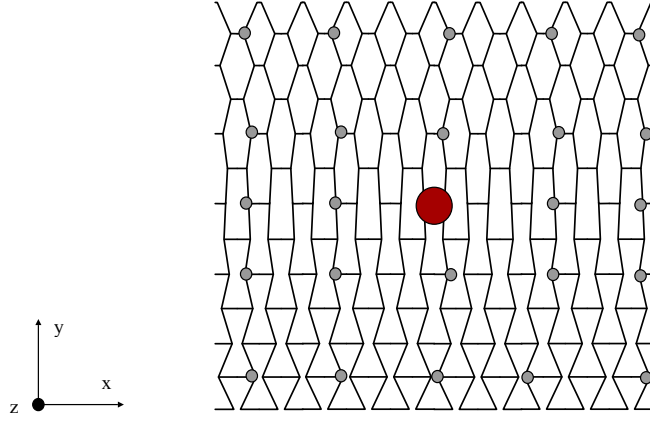
Figure 5: Locations of the measurement points and central clamp for sample 2.
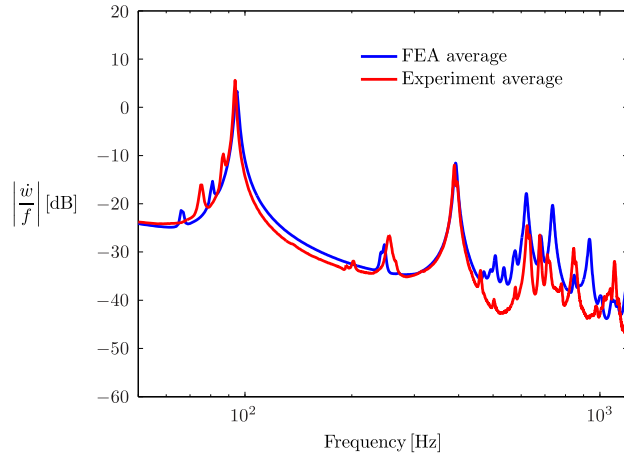
Figure 6: Comparison between experimental and numerical results for the magnitude of the average mobility in sample #1 between the 50 Hz- 1200 Hz frequency bandwidth.
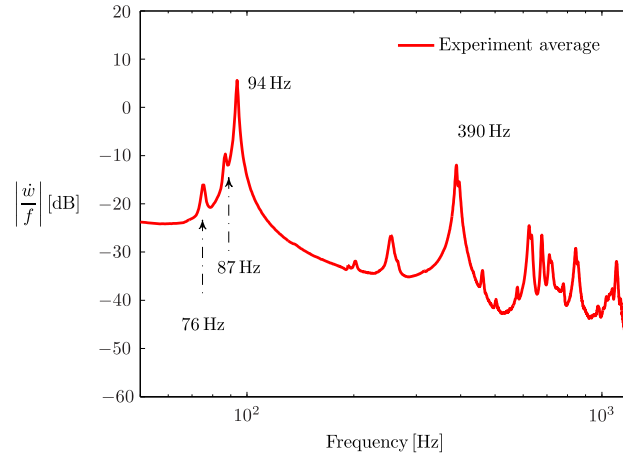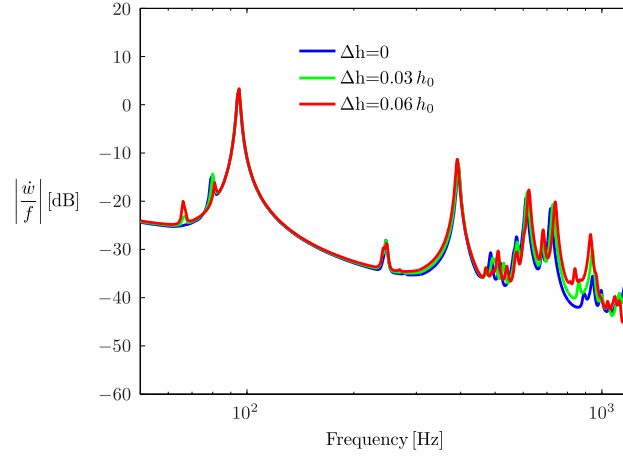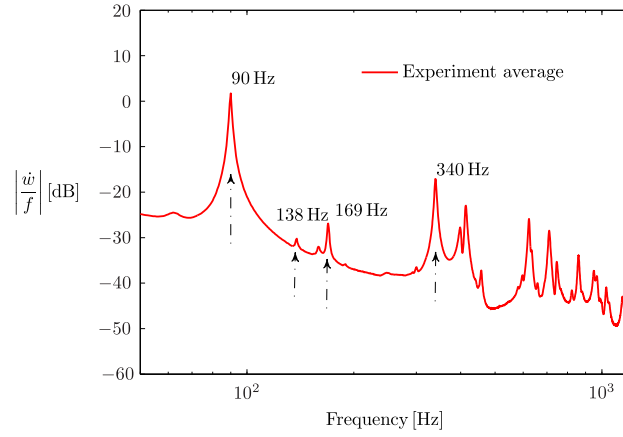
Figure 7: Experimental results for the average mobility magnitude of sample #1 within the 50 Hz-1200 Hz frequency bandwidth.
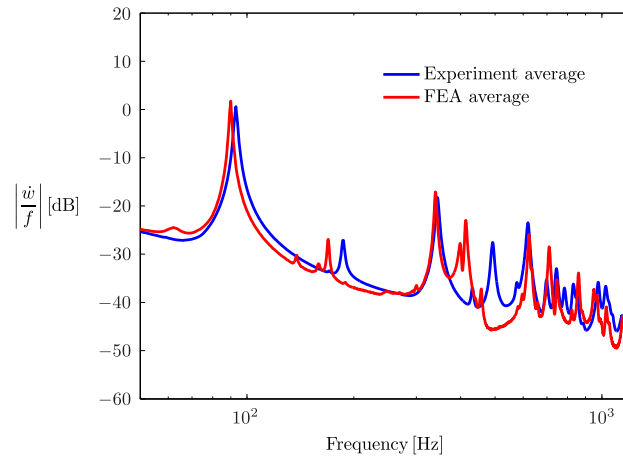
Figure 8: Experimental and numerical results for the magnitude of the average mobility in sample #2 within the 50 Hz - 1200 Hz bandwidth.

Figure 9: Averaged mobility magnitude from different aspect-ratio in topologies #1 with $\Delta h = 0$, $\Delta h = 0.03\,h_0$ and $\Delta h = 0.06\,h_0$.

Figure 10: Experimental results for the average mobility magnitude of sample #2 within the 50-1200 Hz bandwidth.
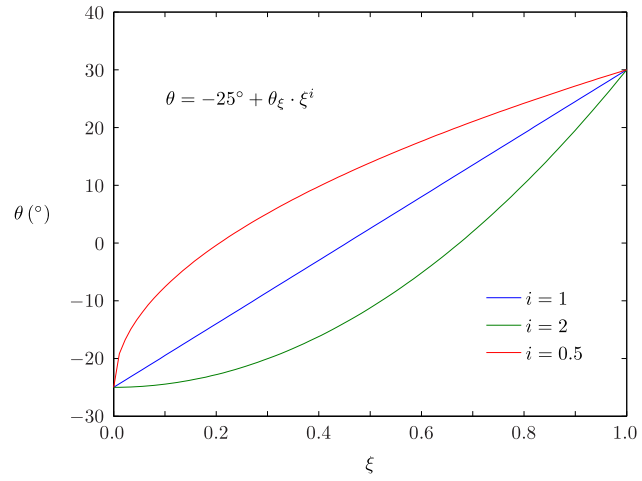
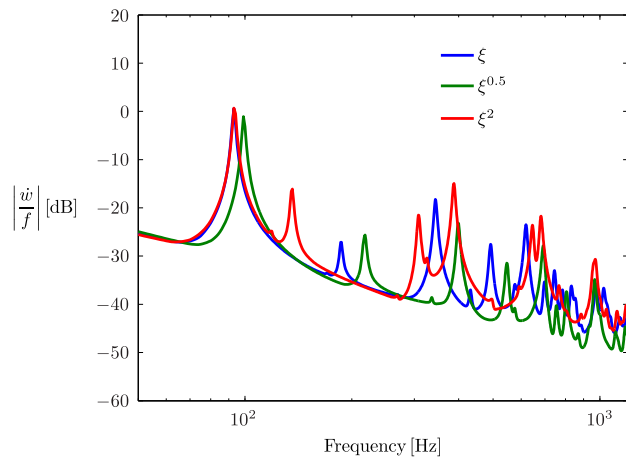Figure 11: Gradient laws for the angle-graded topology #2.

Figure 12: Averaged mobility for different angle-graded topologies #2 with ξ, $\xi^{0.5}$ and ξ^2 as gradient laws (Fig. 4).
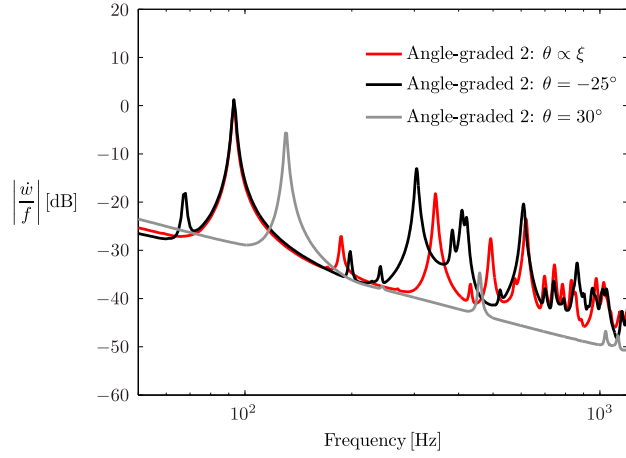
Figure 13: Averaged mobility magnitude of angle-graded linear topology ($\theta \propto \xi$) and periodic topologies with $\theta = -25°$ and $\theta = 30°$.
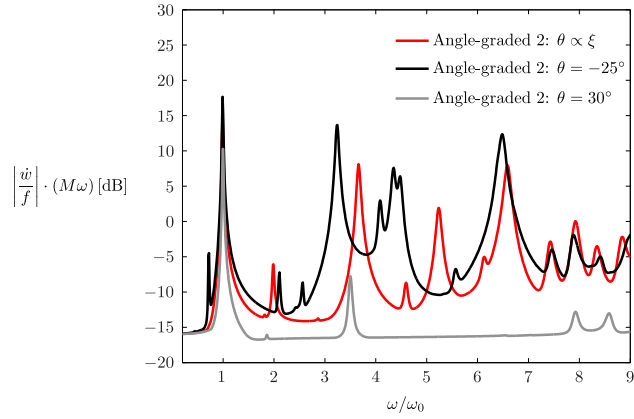

Figure 14: Average normalised mobility for the angle-graded linear topology ($\theta \propto \xi$) and periodic configurations with $\theta = -25°$ and $\theta = 30°$. Frequencies are normalised against ω_0. The mobility is normalized with the panel mass M and the excitation frequency ω.